Title

Integrated Reference Cavity for Dual-mode Optical Thermometry and Frequency Stabilization

Authors

Zhao, Qiancheng

Harrington, Mark W

Isichenko, Andrei

et al.

Publication Date

2021-05-24

OPTICA

Integrated reference cavity with dual-mode optical thermometry for frequency correction

Qiancheng Zhao,[1] Mark W. Harrington,[1] Andrei Isichenko,[1] Kaikai Liu,[1] Ryan O. Behunin,[2,3] Scott B. Papp,[4] Peter T. Rakich,[5] Chad W. Hoyt,[6] Chad Fertig,[6] and Daniel J. Blumenthal[1,*]

[1]Department of Electrical and Computer Engineering, University of California, Santa Barbara, Santa Barbara, California 93106, USA
[2]Department of Applied Physics and Material Science, Northern Arizona University, Flagstaff, Arizona 86011, USA
[3]Center for Materials Interfaces in Research and Applications (¡MIRA!), Northern Arizona University, Flagstaff, Arizona 86011, USA
[4]Time and Frequency Division 688, National Institute of Standards and Technology, Boulder, Colorado 80305, USA
[5]Department of Applied Physics, Yale University, New Haven, Connecticut 06511, USA
[6]Honeywell Aerospace, Plymouth, Minnesota 55441, USA
*Corresponding author: danb@ucsb.edu

Received 24 May 2021; revised 21 September 2021; accepted 3 October 2021 (Doc. ID 432194); published 17 November 2021

Photonic integrated resonators have advantages over traditional benchtop cavities in terms of size, weight, and cost with the potential to enable applications that require spectrally pure light. However, integrated resonators suffer from temperature-dependent frequency variations and are sensitive to external environmental perturbations, which hinders their usage in precision frequency applications. One solution is to use interrogation of the cavity temperature through dual-mode optical thermometry (DMOT) by measuring the shift of the resonance frequency difference between two polarization or optical frequency modes. Yet this approach has only been demonstrated in bulk-optic whispering gallery mode and fiber resonators. In this paper, we implement dual-mode optical thermometry in an ultra-high Q integrated silicon nitride resonator. A dual-mode resonance frequency difference temperature sensitivity of 188 ± 15 MHz/K is measured. We demonstrate feedforward DMOT frequency correction that, under an applied external temperature ramp, is able to reduce the optical frequency change to 0.31 kHz/s as compared to an uncorrected 10.03 kHz/s, a factor of 30× reduction. These results show promise for on-chip frequency correction solutions for quantum, metrology, atomic, and coherent optical communications applications.

https://doi.org/10.1364/OPTICA.432194

1. INTRODUCTION

Optical reference cavities [1–7] play a critical role in laser linewidth narrowing and frequency stabilization for applications including optical communications [8–10], atomic clocks [11–14], spectroscopy [15,16], and quantum computation [17,18]. Laser stabilization techniques that incorporate Pound–Drever–Hall (PDH) locking [19] utilize high-quality factor (Q) bench-top vacuum-spaced Fabry–Perot reference cavities that are composed of single-crystal silicon [3,20] or ultra-low expansion (ULE) glass [5] spacers to achieve better than 10^{-15} fractional frequency stability over a second. For low-cost and portable applications, it is desirable to miniaturize these cavities using photonic integrated waveguide-based technologies. Optical microresonators are a good candidate due to their compact size and reduced sensitivity to environmental disturbances. Bulk-optic resonators based on silica [4] and crystalline fluoride materials [1,2,21] are widely used due to their ultra-high Q factors and high finesse. Recently, bulk-optic vacuum cavities with lithographically defined silica mirrors have achieved finesse over 700,000 [22]. By leveraging recent breakthroughs in ultra-low-loss waveguide fabrication technique, all-waveguide silicon nitride (Si_3N_4) ring resonators have approached 422 million intrinsic Q [23] and 720 million intrinsic Q [24]. These integrated all-waveguide resonators have the advantage of monolithic integration with other components to realize wafer-scale, CMOS compatible, planar lightwave circuits [25], opening the door to high-performance on-chip frequency correction.

A major challenge with waveguide-based integrated resonators is their sensitivity to thermal fluctuations compared to vacuum spaced counterparts as well as to outside environmental disturbances. Cavity frequency deviations occur due to thermorefractive and thermal expansion effects induced by local thermodynamic temperature fluctuations and environmental changes, and can be mitigated by engineering the thermorefractive coefficients [26] or suppressed using a low-expansion substrate [6]. Another approach is active control or correction of the laser frequency using high-sensitivity cavity temperature measurements through differential shifts in the cavity resonant frequencies. Dual-mode optical thermometry (DMOT) has been demonstrated to probe the cavity temperature by detecting the difference in thermal responses

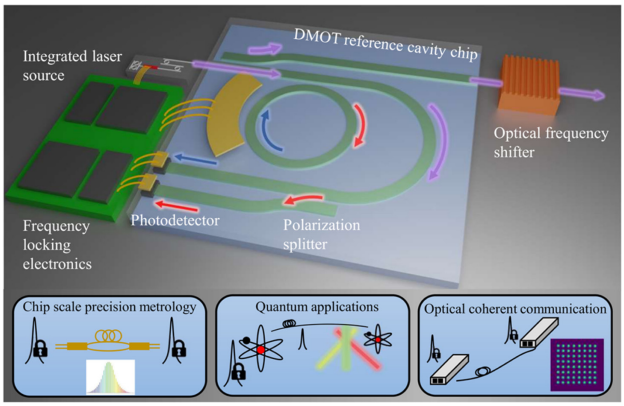

Fig. 1. Illustration of a DMOT temperature reference cavity with an integrated laser locked to the DMOT reference cavity. The DMOT dual-mode difference frequency is monitored for temperature changes and corrects the laser frequency accordingly through control of a cavity heater or optical frequency shifter. Potential applications include precision metrology, quantum, and energy-efficient coherent optical communications.

between two polarization [27] or two frequency [28] modes. The measured intra-cavity temperature is used as an error signal for feedback control to stabilize the cavity temperature [29] or with feedforward control to correct the laser frequency [30]. Advances in miniaturizing the DMOT approach includes crystalline whispering gallery mode (WGM) resonators [31] and fiber resonators [32]. However, to the authors' knowledge, DMOT-based laser frequency correction has not been realized in a photonic integrated waveguide resonator.

Here, we demonstrate DMOT-based temperature measurement and frequency correction using a photonic integrated all-waveguide circuit. The integrated optical reference cavity is composed of an ultra-low-loss Si_3N_4 waveguide design that supports transverse electric (TE) and transverse magnetic (TM) modes, with intrinsic Q factors of 34×10^6 and 170×10^6, respectively. We measure a dual-mode difference frequency temperature sensitivity of 188 ± 15 MHz/K, which is the response of the resonance frequency difference between the TE and TM modes as a function of temperature change. A tunable semiconductor laser is locked to the DMOT TE and TM modes using sideband modulation and dual PDH loops. The measured frequency difference is employed as a feedforward frequency correction signal [30], which is chosen to overcome limitations of the control loop delay in a feedback on the cavity temperature. In the presence of an external linear temperature ramp change and with feedforward correction, the output frequency change rate is reduced to 0.31 kHz/s compared to 10.03 kHz/s without correction, representing a ~30× factor improvement.

An artistic illustration of a photonic circuit that employs a DMOT integrated cavity is shown in Fig. 1. The TE and TM modes of a laser are locked to the DMOT cavity resonances and the dual-mode difference frequency, which is a measure of the cavity temperature, is processed by an electronic circuit that corrects the output laser frequency via a laser cavity heater or single sideband optical frequency modulator.

2. RESULTS

The DMOT is schematically shown in Fig. 2(a) and consists of 80 nm × 6 μm silicon nitride waveguide cores surrounded by oxide cladding that support both TE and TM polarization modes. A dual-mode all-pass ring resonator has a radius of 8530.8 μm and a 3.5 μm bus–ring coupling gap that couples both TE and TM modes [Fig. 2(a)]. The resonator [Fig. 2(b)] is fabricated using an ultra-low-loss Si_3N_4 waveguide-fabrication technique [23] (see Supplement 1 for details). The TE and TM modes have different mode areas and waveguide confinement factors, leading to a difference in the effective thermo-optic coefficients. This results in a cavity temperature-dependent resonance frequency difference between the modes. Therefore, the modal resonance frequency difference is a read-out of the cavity temperature.

A. Dual-Mode Resonator Characteristics

The resonator transmission spectrum, linewidths and Qs for both TE and TM modes are characterized (see Fig. 3). The TE mode free spectral range (FSR) is measured to be 3.63 and 3.76 GHz for the TM mode [Fig. 3(a)]. We use these values to calculate the waveguide group index $n_{g,TM} = 1.49$ for the TM mode and $n_{g,TE} = 1.54$ for the TE mode, both at 1550 nm. The TE and TM mode loaded Q factors are measured using two different techniques: a radio frequency (RF) calibrated Mach–Zehnder interferometer (MZI) method and a ring-down method (see Supplement 1 for details). The full width at half maximum (FWHM) of the TM resonance [Fig. 3(b)] is $\Delta\nu_{TM} = 22.50$ MHz, yielding a loaded Q factor $Q_{L,TM} = 9 \times 10^6$ at 1550 nm through curve fitting (see Supplement 1 for further detail). The small asymmetric feature from the TM resonance [Fig. 3(b)] could be from absorption-related loss [23,33]. Similarly, the TE mode [Fig. 3(c)] FWHM is measured to be $\Delta\nu_{TE} = 5.86$ MHz with a calculated loaded Q factor $Q_{L,TE} = 33 \times 10^6$, with slight broadening that

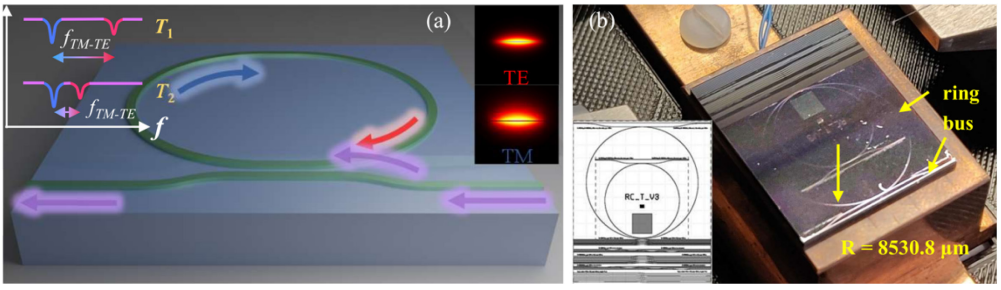

Fig. 2. (a) Artistic illustration of a dual-mode optical thermometry-based silicon nitride reference cavity. The red, blue, and purple colors represent the TE mode, TM mode, and combined polarizations, respectively. The optical mode profiles of the two polarizations are shown in the top-right. (b) An artistically enhanced photo of the fabricated device. Other structures can also be observed on same die, including a smaller ring resonator, waveguide coupler test structures, and an etch monitor square. The inset shows the die layout.

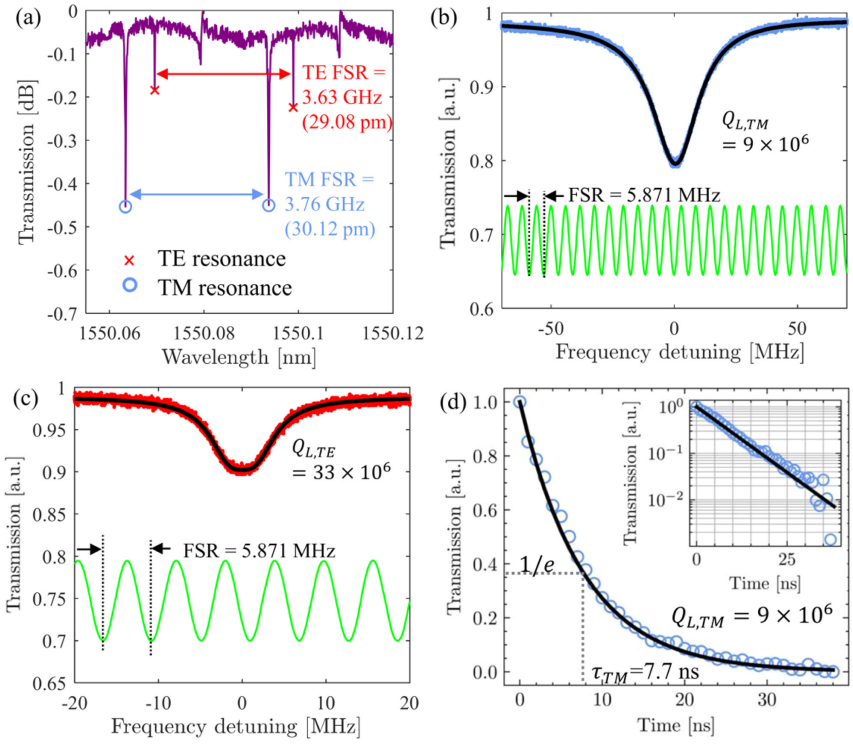

Fig. 3. DMOT cavity free-spectral range (FSR), linewidth, and ring-down measurements. (a) FSR measurement of the transverse magnetic (TM) and transverse electric (TE) mode resonances. The TM and TE mode resonances are denoted by the blue "◯" and red "×" signs. The FSRs of the TM and TE modes are 3.76 and 3.63 GHz, respectively. (b) Transmission spectrum of the TM resonance at 1550 nm. The loaded quality (Q) factor is derived from the full width half maximum (FWHM). An unbalanced Mach–Zehnder Interferometer (MZI) with FSR of 5.871 ± 0.004 MHz (green curve) is used to calibrate the frequency detuning. (c) Transmission spectrum of the TE mode with its FWHM and the loaded Q factor denoted. (d) Ring-down measurement of the TM resonance results in a cavity lifetime of 7.7 ns, corresponding to a loaded Q factor (Q_L) of 9 million. A first-order exponential decay function (black solid line) is fit to the normalized resonator transmission output (circle), and the time stamp corresponding to the $1/e$ point (where $e \approx 2.71828$) is extracted as the TM mode ring-down time. The ring-down time, τ, and the $1/e$ transmission are indicated by the gray dashed lines. Inset shows the transmission output (circle) in logarithmic scale, and the solid line shows the fitting of the data.

can also be due to typical effects such as asymmetric mode splitting and losses [23,33]. The loaded TM Q factor is also measured using the ring-down method [23,34]. A decay time (τ_{TM}) of 7.7 ns is measured and a calculated loaded Q factor $\sim 9 \times 10^6$ is in agreement with the MZI measurement [Fig. 3(d)]. The ring-down method was not performed for the TE mode due to the small extinction ratio that degrades the signal-to-noise ratio (SNR). Using the loaded Q factors and the group indices, the TM and TE mode waveguide propagation losses are calculated to be 0.2 and 0.8 dB/m, respectively (see Supplement 1 for details). The TM mode propagation loss is lower due to lower scattering loss from the top waveguide surface compared to TE sidewall scattering loss [23]. The intrinsic Q factors of the TM and TE modes are calculated to be 170×10^6 and 34×10^6, respectively (see Supplement 1 for details). The ring–bus coupling gap was designed to support different optical mode areas and propagation losses for the TM and TE modes, with an over-coupled TM resonance and under-coupled TE resonance. This design tradeoff results in reduced extinction ratios for both resonances. The characteristics of the TE and TM modes are summarized in Table 1.

Table 1. Summary of TE and TM Resonance Characteristics

Mode	Q_L (×10^6)	Q_{int} (×10^6)	FWHM [MHz]	Extinction Ratio	FSR [GHz]	n_g	α [dB/m]
TM	9	170	22.50	1.24	3.76	1.49	0.2
TE	33	34	5.86	1.09	3.63	1.54	0.8

B. Dual-Mode Difference Frequency Temperature Sensitivity

The linearized temperature dependence for a mode with resonance frequency f can be related to the thermal expansion and thermorefractive effects in a dielectric waveguide resonator as described by Eq. (1) [35]:

$$\frac{1}{f}\frac{df}{dT} + \frac{1}{n_g}\frac{dn_{\text{eff}}}{dT} + \frac{n_{\text{eff}}}{n_g}\alpha_E = 0, \tag{1}$$

where n_{eff} is the effective mode refractive index, n_g is the group index, α_E is the linear thermal expansion coefficient, and $\mathrm{d}n_{\text{eff}}/\mathrm{d}T$ is the effective thermo-optic coefficient of the waveguide mode. The temperature sensitivity, as measured by the resonant frequency difference between the TE and TM modes, is given by Eq. (2) assuming the polarization modes have large spatial overlap (i.e., $\alpha_{\text{E}}^{\text{TE}} \approx \alpha_{\text{E}}^{\text{TM}}$):

$$\frac{df_{\text{TM-TE}}}{dT} = -f\left[\left(\frac{1}{n_g^{\text{TM}}}\frac{dn_{\text{eff}}^{\text{TM}}}{dT} - \frac{1}{n_g^{\text{TE}}}\frac{dn_{\text{eff}}^{\text{TE}}}{dT}\right) + \left(\frac{n_{\text{eff}}^{\text{TM}}}{n_g^{\text{TM}}} - \frac{n_{\text{eff}}^{\text{TE}}}{n_g^{\text{TE}}}\right)\alpha_{\text{E}}\right]. \tag{2}$$

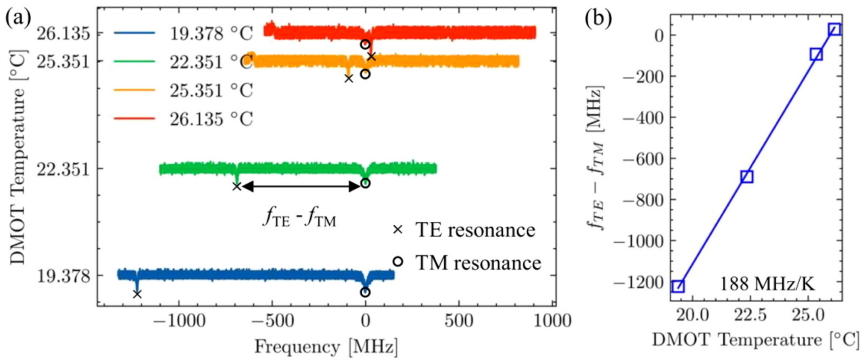

Fig. 4. (a) DMOT cavity transverse electric (TE) and transverse magnetic (TM) resonance peak locations at various DMOT temperatures with difference frequency $f_{TE} - f_{TM}$ indicated. The TM resonance also changes as a function of temperature; however, here it is normalized to zero offset in order to measure and quantify the frequency difference. (b) Difference resonance frequency as a function of DMOT temperature with linear fit to calibrate the measurement temperature sensitivity.

Using the measured thermo-optic coefficients for Si_3N_4 and SiO_2 at 1550 nm as $24.5 \times 10^{-6}\ K^{-1}$ [36] and $9.8 \times 10^{-6}\ K^{-1}$ [37] respectively, we calculate $dn_{\text{eff}}^{\text{TM}}/dT$ to be $9.9 \times 10^{-6}\ K^{-1}$ and $dn_{\text{eff}}^{\text{TE}}/dT$ to be $11.2 \times 10^{-6}\ K^{-1}$. The corresponding dual-mode difference frequency temperature sensitivity, denoted by $d|\ f_{TM} - f_{TE}|/dT$, is calculated to be 153 MHz/K. Since the optical mode is weakly guided and a large portion of the optical power propagates in the SiO_2 cladding, it is reasonable to use the linear thermal expansion coefficient of amorphous SiO_2, which is $0.56 \times 10^{-6}\ K^{-1}$ [38], as an approximation for the linear thermal expansion coefficient of the composite waveguide. Using Eq. (1), the TM mode resonance frequency temperature sensitivity $d\,f_{TM}/dT$ is calculated to be 1387 MHz/K. We experimentally calibrate $d|\ f_{TM} - f_{TE}|/dT$ by measuring the resonance frequencies of the TE and TM modes as a function of the DMOT resonator temperature, as shown in Fig. 4(a). For temperature control, we use a SLICE-QT from Vescent Photonics that is specified with ±0.2 mK stability over 1 h and a temperature setpoint precision of 0.1 mK. Details of the mechanical and thermal assembly are given in Supplement 1. The TE and TM resonance peaks are indicated at each DMOT temperature as well as their frequency difference $f_{TE} - f_{TM}$. These measurements are summarized in the plot of $f_{TE} - f_{TM}$ as a function of the DMOT temperature in Fig. 4(b). A linear fit yields a dual-mode frequency difference temperature sensitivity $d|\ f_{TM} - f_{TE}|/dT = 188 \pm 15$ MHz/K. The difference from the theoretical value given by Eq. (1) is most likely due to variations in the actual material and waveguide properties from the assumed values.

C. Dual-Mode Temperature Measurement and Optical Frequency Correction

The feedforward optical frequency correction approach is shown schematically in Fig. 5. The TE and TM modes of a tunable laser output are independently locked to the TE and TM resonances of the DMOT cavity using separate PDH lock loops as indicated by the blue and red paths in Fig. 5. The laser output frequency tracks the TM resonance using a proportional-integral-derivate (PID) control signal fed back to the tunable semiconductor laser. An electro-optic modulator (EOM) generates a tunable optical sideband from the laser carrier and, in combination with a voltage controlled oscillator (EOM-VCO), is used to lock the sideband to the TE mode. Temperature changes in the DMOT cavity lead to changes in the TE and TM mode resonance frequencies, and the EOM-VCO signal proportionally tracks the differential mode frequency difference $|f_{TM} - f_{TE}|$ which is a function of the DMOT cavity temperature, $F_2(T_{\text{cavity}})$. The laser output frequency, also a function of the cavity temperature $F_1(T_{\text{cavity}})$, is input to a frequency shifting acousto-optic modulator (AOM). The EOM-VCO output is scaled with a negative feedforward gain block that has been calibrated to counteract the temperature-induced frequency shift of the laser output, resulting in the frequency-corrected optical signal (green arrow).

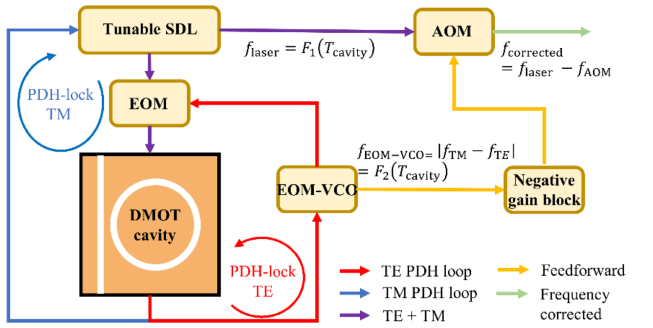

Fig. 5. Dual-mode lock and frequency correction system. DMOT cavity is held at programmable temperature T_{cavity}. Tunable laser output (purple line) TM polarization component is PDH locked (blue loop) to DMOT TM resonance and TE polarization component is locked (red loop) to DMOT TE resonance. TM PDH loop lock tunes the tunable laser carrier frequency using a PID current control while TE PDH loop lock tunes a sideband generated by the EOM. The EOM-VCO that drives the TE sideband also generates the difference frequency $|f_{TM} - f_{TE}|$ that is input to a negative gain block (yellow path) that is calibrated to cancel the temperature-induced DMOT resonance shift. The negative feedforward signal is used to drive the output AOM and shift the tunable laser output back to a corrected optical frequency (green arrow).

Further details of the experimental setup are shown in Fig. 6(a), with the TE and TM mode PDH lock loops (red and blue dotted lines) and the frequency correction feedforward circuit (yellow dotted lines). The TM and TE mode transmission spectra and their error signals are depicted in Fig. 6(b), with each measurement trace labeled as (1), (2), (3), and (4) in relation to location in Fig. 6(a). The purple arrows in Fig. 6(b) identify the dual-mode difference frequency $f_{\text{EOM-VCO}} = |f_{TM} - f_{TE}|$. A PDH error signal with high SNR requires sufficient input optical power for tight locking.

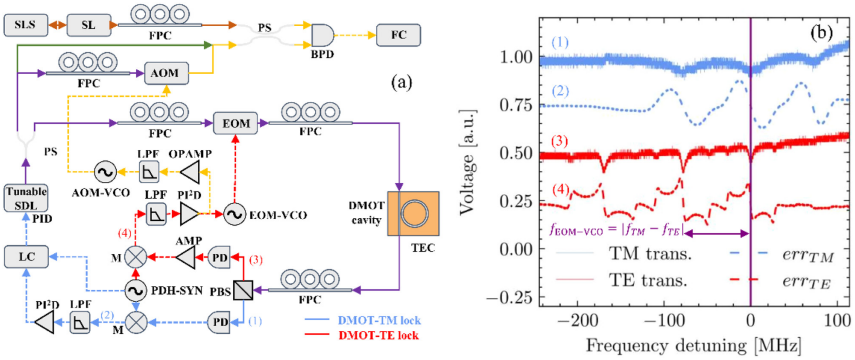

Fig. 6. (a) Dual-mode optical thermometry feedforward stabilization system diagram. Solid lines represent optical paths, and dashed lines represent electrical paths. Blue color is related to optical transverse magnetic (TM) mode, and red color is related to optical transverse electric (TE) mode. Purple path includes both TE and TM modes. Yellow path is used for feedforward stabilization. Green solid line is the optical path that bypasses the acousto-optic modulator (AOM). The AOM is bypassed in the temperature sensitivity experiment but is engaged in the frequency stabilization experiment. SDL, laser; LC, laser controller; PI^2D, proportional-integral-differential controller; LPF, low-pass filter; M, mixer; PDH-SYN, RF synthesizer for PDH locking; PD, photodetector; PBS, polarization beam splitter; FPC, fiber polarization controller; VCO, voltage controlled oscillator; TEC, thermoelectric cooler; AMP, RF amplifier; OPAMP, operational amplifier; FC, frequency counter; EOM, electro-optic modulator; AOM, acousto-optic modulator; SLS, stable laser system reference cavity; PS, 50:50 power splitter; BPD, balanced photodetector. (b) TM (blue) and TE (red) transmission spectra (solid lines) and their PDH error signals (dashed lines). The probing locations of the measured signals are labeled as (1), (2), (3), and (4) in (a). Purple solid line shows the locked laser frequency position.

We estimate the on-chip optical power to be 1.3 and 0.7 mW for the TE and TM modes, respectively. Using the feedforward error signal [yellow dotted line in Fig. 6(a)], the output frequency of SDL is corrected by shifting the output frequency of an AOM with the negative proportional AOM-VCO signal. The error signal that drives the EOM-VCO is also input to an operational amplifier (OPAMP) with adjustable gain, whose output voltage is used to control the AOM-VCO, which in turn drives the frequency shift of the AOM [yellow dashed line in Fig. 6(a)]. The OPAMP gain is optimized so that the change of the AOM frequency-shifted output is equal and opposite sign to the change of the laser frequency, providing the frequency-corrected output.

Optical frequency variations are measured by photomixing either the uncorrected (green trace) or corrected (yellow trace) signals with a reference stabilized laser (SL) and measuring the heterodyne beatnote with a frequency counter. The SL consists of a fiber laser stabilized to an ultra-stable Fabry–Perot cavity made of ULE glass (HV-6020-4, Stable Laser Systems, Boulder, CO) which serves as a reference laser oscillator for this measurement. The SLS cavity has a linewidth of 1.55 kHz and <5 kHz/day(∼ 0.1 Hz/s) frequency drift at 1550 nm. Therefore the SL frequency change rate is several orders of magnitude lower than that of the DMOT feedforward frequency correction.

D. Feedforward Gain Calibration

In the output stage (see Fig. 5), the AOM is controlled by a signal that drives a frequency shift in an equal and opposite direction to that of the temperature-induced laser frequency shift. The control signal that drives the EOM-VCO is calibrated and scaled in order to produce the correct feedforward signal and AOM-VCO frequency response. The ability to accurately correct the optical frequency depends on this linear scaling calibration and uncertainty in the scaling and noise sources in the feedforward path. We measure the mode difference frequency and laser frequency as a function of cavity temperature (Fig. 7). The laser frequency at the input to the AOM [green path in Fig. 5(a)] yields the response of the temperature-driven laser frequency variation and its temperature sensitivity. The mode frequency difference $|f_{TM} - f_{TE}|$ is measured with a frequency counter and plotted as a function of the thermoelectric cooler (TEC) temperature in Fig. 7(a). A linear curve fit yields a sensitivity of 181 MHz/K. The 4% difference between this value and the open loop value in Fig. 4(b) may be due to the operation of the dual-lock loops. The laser frequency is plotted with respect to the TEC set temperature in Fig. 7(b), yielding a slope of 1588 MHz/K. The data from Figs. 7(a) and 7(b) are combined to generate f_{laser} as a function of $|f_{TM} - f_{TE}|$ [Fig. 7(c)]. A linear fit returns a slope of 8.7, which is used to set the feedforward path gain.

E. Laser Frequency Correction

We demonstrate the use of this approach to correct changes in the output optical frequency in the presence of a continuous temperature change. A 6.3 μK/s linear temperature ramp is applied to the DMOT cavity with ΔT per time plotted (purple line in upper plot, Fig. 8). The EOM-VCO output frequency, which is a function of DMOT cavity temperature, is plotted as a function of time (green line in upper plot, Fig. 8). Over the first 240 s of the temperature change, without the feedforward path engaged, the output optical frequency measured as the beatnote between the AOM output and the SL is shown in the blue trace in the lower plot, left side un-shaded region, of Fig. 8. A linear fit (magenta dashed line) to this data yields an output frequency change without feedforward correction of −10.03 kHz/s. The calibrated DMOT feedforward signal is engaged at that AOM at 240 s, in the presence of the continued increasing temperature ramp. The corrected laser frequency in the presence of the temperature ramp is shown in the blue curve of the lower plot in the right side shaded region of Fig. 8. The output frequency is corrected to within −0.31 kHz/s (linear fit orange dashed line), a 30× reduction in frequency change over the uncorrected signal.

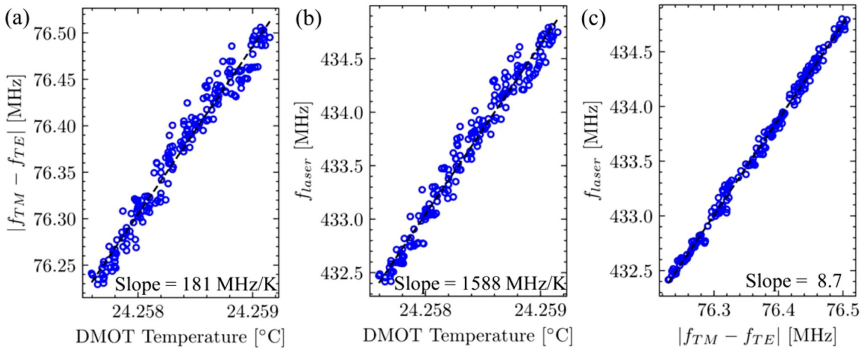

Fig. 7. Feedforward gain calibration curves. (a) $|f_{\mathrm{TM}} - f_{\mathrm{TE}}|$ versus TEC temperature. (b) f_{laser} versus TEC temperature. (c) f_{laser} versus $|f_{\mathrm{TM}} - f_{\mathrm{TE}}|$.

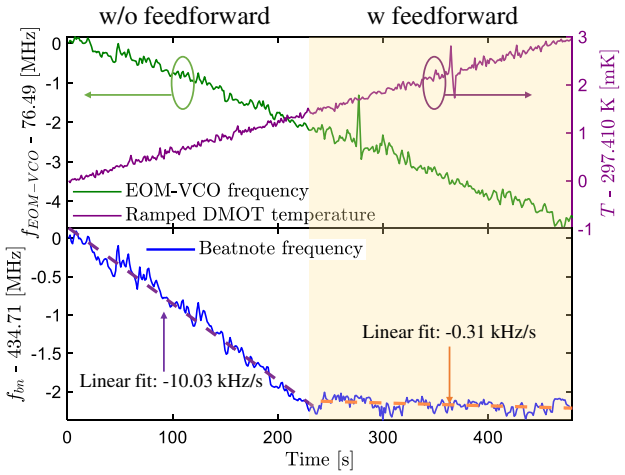

Fig. 8. Upper plot, purple trace: a 6.3 μK/s linear temperature ramp applied to the dual-mode optical thermometry (DMOT) cavity. Upper plot, green trace: EOM-VCO output frequency. Lower plot, blue trace: output optical frequency measured as the beatnote between the AOM output and the SL. Lower plot, left side unshaded, 0–240 s: output with no feedforward frequency correction. Lower plot, right side shaded, 240–480 s: output with feedforward frequency correction. Lower plot, magenta dashed line: linear fit to measured beatnote frequency without feedforward correction of −10.03 kHz/s. Lower plot, orange dashed line: linear fit to measured beatnote frequency with feedforward correction of −0.31 kHz/s.

3. DISCUSSION AND CONCLUSION

We have demonstrated dual-mode optical thermometry (DMOT) in an integrated, all-waveguide Si_3N_4 reference cavity. The reference cavity supports dual TE and TM modes with measured intrinsic Qs of 34 million and 170 million, respectively. Based on the relative frequency shift of the modes as a function of temperature, a sensitivity of 188 ± 15 MHz/K is measured. We demonstrate the use of the DMOT as a temperature sensor with feedforward optical frequency correction in the presence of an external temperature ramp (6.3 μK/s). The output frequency change is corrected to −0.31 kHz/s with the feedforward signal engaged, compared to −10.03 kHz/s without feedforward correction, a reduction of ∼30×.

The waveguide-based DMOT has design tradeoffs that can be addressed in the future, including the selection of TE/TM mode overlap and regulation of the cavity input optical power. This design utilizes the differential thermal response of the TE and TM modes to sense the cavity temperature while suppressing the common noise with a calculated ∼63% mode overlap. The cavity's volumetric heat capacity, which describes the inertia to thermal fluctuations per volume, is similar to those of fiber and ULE glass resonators but smaller than $LiNbO_3$ and MgF_2 resonators (see Supplement 1 for details). Since the TE and TM modes do not overlap with the same waveguide cross section and materials, one of the modes can measure temperature gradients caused by temperature effects at the surface if that mode is overlapped more with the surface region than the other mode. In this case, the two modes do not see the same temperature changes, e.g., at the chip surface, and the DMOT temperature accuracy is reduced, which can be improved by mode engineering. Another limitation is the resonance peak frequency tracking and noise sources in the feedback and feedforward paths. The performance of the feedforward-corrected laser frequency is set by (1) the minimum resolution of the separation between the dual resonances and the cavity linewidths of the two resonances, and (2) the ability to minimize all other non-temperature related effects that influence the resonance separation. We believe that feedforward correction suffers from non-temperature-related noise and other noise sources that are difficult to compensate for. While we did not characterize the noise properties in this paper, we believe accurate accounting of all noise sources can lead to improvements in frequency correction performance. In the future, improvements can include suppression of vibrations, intensity, and electronic noise with improved packaging and environmental isolation. Resonators with higher loaded Q factors for both polarizations can improve sensitivity as well as integrating the dual-mode sensor into the laser cavity [7,30]. This work demonstrates integration of DMOT techniques at the chip scale and application to frequency correction in the presence of external environmental temperature changes.

Funding. Advanced Research Projects Agency–Energy (DE-AR0001042); Defense Advanced Research Projects Agency (FA9453-19-C-0030).

Acknowledgment. The authors would like to thank Naijun Jin from Yale University for constructive discussions on dual-mode optical thermometry system modeling, and Luke Theogarajan and Akshar Jain from the University of California at Santa Barbara for providing test equipment. A portion of the work was performed in the UCSB Nanofabrication Facility, an open access laboratory. Andrei Isichenko acknowledges support from the National Defense Science and Engineering Graduate (NDSEG) Fellowship Program. The views and conclusions contained in this document are those of the authors and should not be interpreted as representing official policies of DARPA, ARPA-E, or the U.S. Government or any agency thereof.

Disclosures. The authors declare no conflicts of interest.

Data availability. The data that support the plots within this paper and other findings of this study are available from the corresponding author on reasonable request.

Supplemental document. See Supplement 1 for supporting content.

REFERENCES

1. A. B. Matsko, A. A. Savchenkov, N. Yu, and L. Maleki, "Whispering-gallery-mode resonators as frequency references. I. Fundamental limitations," J. Opt. Soc. Am. B **24**, 1324–1335 (2007).
2. A. A. Savchenkov, A. B. Matsko, V. S. Ilchenko, N. Yu, and L. Maleki, "Whispering-gallery-mode resonators as frequency references. II. Stabilization," J. Opt. Soc. Am. B **24**, 2988–2997 (2007).
3. T. Kessler, C. Hagemann, C. Grebing, T. Legero, U. Sterr, F. Riehle, M. J. Martin, L. Chen, and J. Ye, "A sub-40-mHz-linewidth laser based on a silicon single-crystal optical cavity," Nat. Photonics **6**, 687–692 (2012).
4. H. Lee, M.-G. Suh, T. Chen, J. Li, S. A. Diddams, and K. J. Vahala, "Spiral resonators for on-chip laser frequency stabilization," Nat. Commun. **4**, 2468 (2013).
5. S. Häfner, S. Falke, C. Grebing, S. Vogt, T. Legero, M. Merimaa, C. Lisdat, and U. Sterr, "8×10^{-17} fractional laser frequency instability with a long room-temperature cavity," Opt. Lett. **40**, 2112–2115 (2015).
6. J. Lim, A. A. Savchenkov, E. Dale, W. Liang, D. Eliyahu, V. Ilchenko, A. B. Matsko, L. Maleki, and C. W. Wong, "Chasing the thermodynamical noise limit in whispering-gallery-mode resonators for ultrastable laser frequency stabilization," Nat. Commun. **8**, 8 (2017).
7. S. Gundavarapu, G. M. Brodnik, M. Puckett, T. Huffman, D. Bose, R. Behunin, J. Wu, T. Qiu, C. Pinho, N. Chauhan, J. Nohava, P. T. Rakich, K. D. Nelson, M. Salit, and D. J. Blumenthal, "Sub-hertz fundamental linewidth photonic integrated Brillouin laser," Nat. Photonics **13**, 60–67 (2019).
8. S. Manipatruni, R. K. Dokania, B. Schmidt, N. Sherwood-Droz, C. B. Poitras, A. B. Apsel, and M. Lipson, "Wide temperature range operation of micrometer-scale silicon electro-optic modulators," Opt. Lett. **33**, 2185–2187 (2008).
9. D. J. Blumenthal, "Ultra-stable integrated lasers and low-cost, low-energy coherent data center interconnect," in *OSA Advanced Photonics Congress (AP) 2019 (IPR, Networks, NOMA, SPPCom, PVLED)* (Optical Society of America, 2019), paper NeM4D.1.
10. G. M. Brodnik, M. W. Harrington, J. H. Dallyn, D. Bose, W. Zhang, L. Stern, P. A. Morton, R. O. Behunin, S. B. Papp, and D. J. Blumenthal, "Optically synchronized fibre links using spectrally pure chip-scale lasers," Nat. Photonics **15**, 588–593 (2021).
11. Y. Y. Jiang, A. D. Ludlow, N. D. Lemke, R. W. Fox, J. A. Sherman, L.-S. Ma, and C. W. Oates, "Making optical atomic clocks more stable with 10^{-16}-level laser stabilization," Nat. Photonics **5**, 158–161 (2011).
12. B. J. Bloom, T. L. Nicholson, J. R. Williams, S. L. Campbell, M. Bishof, X. Zhang, W. Zhang, S. L. Bromley, and J. Ye, "An optical lattice clock with accuracy and stability at the 10^{-18} level," Nature **506**, 71–75 (2014).
13. A. D. Ludlow, M. M. Boyd, J. Ye, E. Peik, and P. O. Schmidt, "Optical atomic clocks," Rev. Mod. Phys. **87**, 637–701 (2015).
14. N. Chauhan, A. Isichenko, K. Liu, J. Wang, Q. Zhao, R. O. Behunin, P. T. Rakich, A. M. Jayich, C. Fertig, C. W. Hoyt, and D. J. Blumenthal, "Visible light photonic integrated Brillouin laser," Nat. Commun. **12**, 4685 (2021).
15. S. M. Link, D. J. H. C. Maas, D. Waldburger, and U. Keller, "Dual-comb spectroscopy of water vapor with a free-running semiconductor disk laser," Science **356**, 1164–1168 (2017).
16. A. Raza, S. Clemmen, P. Wuytens, M. de Goede, A. S. K. Tong, N. L. Thomas, C. Liu, J. Suntivich, A. G. Skirtach, S. M. Garcia-Blanco, D. J. Blumenthal, J. S. Wilkinson, and R. Baets, "High index contrast photonic platforms for on-chip Raman spectroscopy," Opt. Express **27**, 23067–23079 (2019).
17. A. Orieux and E. Diamanti, "Recent advances on integrated quantum communications," J. Opt. **18**, 083002 (2016).
18. F. Flamini, N. Spagnolo, and F. Sciarrino, "Photonic quantum information processing: a review," Rep. Prog. Phys. **82**, 016001 (2018).
19. E. D. Black, "An introduction to Pound–Drever–Hall laser frequency stabilization," Am. J. Phys. **69**, 79–87 (2000).
20. D. G. Matei, T. Legero, S. Häfner, C. Grebing, R. Weyrich, W. Zhang, L. Sonderhouse, J. M. Robinson, J. Ye, F. Riehle, and U. Sterr, "1.5um lasers with sub-10 mHz linewidth," Phys. Rev. Lett. **118**, 263202 (2017).
21. J. Alnis, A. Schliesser, C. Y. Wang, J. Hofer, T. J. Kippenberg, and T. W. Hänsch, "Thermal-noise-limited crystalline whispering-gallery-mode resonator for laser stabilization," Phys. Rev. A **84**, 011804 (2011).
22. J. P. Hendrie, N. Jin, C. A. McLemore, Y. Luo, M. Kelleher, D. Mason, P. Kharel, F. Quinlan, P. Rakich, and S. A. Diddams, "Versatile microfabricated mirrors with finesse > 700,000," in *Conference on Lasers and Electro-Optics* (Optical Society of America, 2021), paper STh4J.2.
23. M. W. Puckett, K. Liu, N. Chauhan, Q. Zhao, N. Jin, H. Cheng, J. Wu, R. O. Behunin, P. T. Rakich, K. D. Nelson, and D. J. Blumenthal, "422 Million intrinsic quality factor planar integrated all-waveguide resonator with sub-MHz linewidth," Nat. Commun. **12**, 934 (2021).
24. K. Liu, N. Jin, H. Cheng, M. W. Puckett, R. O. Behunin, K. D. Nelson, P. T. Rakich, and D. J. Blumenthal, "380 μW threshold Brillouin lasing in 720 million intrinsic Q photonic integrated resonator," in *Workshop on Optimisation, Metric Bounds, Approximation and Transversality (WOMBAT)* (2021).
25. W. Jin, Q.-F. Yang, L. Chang, B. Shen, H. Wang, M. A. Leal, L. Wu, M. Gao, A. Feshali, M. Paniccia, K. J. Vahala, and J. E. Bowers, "Hertz-linewidth semiconductor lasers using CMOS-ready ultra-high-Q microresonators," Nat. Photonics **15**, 346–353 (2021).
26. Q. Zhao, R. O. Behunin, P. T. Rakich, N. Chauhan, A. Isichenko, J. Wang, C. Hoyt, C. Fertig, M. H. Lin, and D. J. Blumenthal, "Low-loss low thermo-optic coefficient Ta_2O_5 on crystal quartz planar optical waveguides," APL Photon. **5**, 116103 (2020).
27. L. M. Baumgartel, R. J. Thompson, and N. Yu, "Frequency stability of a dual-mode whispering gallery mode optical reference cavity," Opt. Express **20**, 29798–29806 (2012).
28. W. Weng, J. D. Anstie, T. M. Stace, G. Campbell, F. N. Baynes, and A. N. Luiten, "Nano-Kelvin thermometry and temperature control: beyond the thermal noise limit," Phys. Rev. Lett. **112**, 160801 (2014).
29. Q. Zhao, M. W. Harrington, A. Isichenko, G. M. Brodnik, K. Liu, R. O. Behunin, P. T. Rakich, C. W. Hoyt, C. Fertig, S. B. Papp, and D. J. Blumenthal, "Laser frequency drift stabilization using an integrated dual-mode locking Si_3N_4 waveguide reference cavity," in *Conference on Lasers and Electro-Optics* (Optical Society of America, 2021), paper STh2B.7.
30. W. Loh, J. Stuart, D. Reens, C. D. Bruzewicz, D. Braje, J. Chiaverini, P. W. Juodawlkis, J. M. Sage, and R. McConnell, "Operation of an optical atomic clock with a Brillouin laser subsystem," Nature **588**, 244–249 (2020).
31. J. Lim, W. Liang, A. A. Savchenkov, A. B. Matsko, L. Maleki, and C. W. Wong, "Probing 10 μK stability and residual drifts in the cross-polarized dual-mode stabilization of single-crystal ultrahigh-Q optical resonators," Light Sci. Appl. **8**, 1 (2019).
32. W. Loh, S. Yegnanarayanan, F. O'Donnell, and P. W. Juodawlkis, "Ultra-narrow linewidth Brillouin laser with nanokelvin temperature self-referencing," Optica **6**, 152–159 (2019).
33. M. H. P. Pfeiffer, J. Liu, A. S. Raja, T. Morais, B. Ghadiani, and T. J. Kippenberg, "Ultra-smooth silicon nitride waveguides based on the Damascene reflow process: fabrication and loss origins," Optica **5**, 884–892 (2018).
34. K. Y. Yang, D. Y. Oh, S. H. Lee, Q.-F. Yang, X. Yi, B. Shen, H. Wang, and K. Vahala, "Bridging ultrahigh-Q devices and photonic circuits," Nat. Photonics **12**, 297–302 (2018).
35. K. Padmaraju and K. Bergman, "Resolving the thermal challenges for silicon microring resonator devices," Nanophotonics **3**, 269–281 (2014).
36. A. Arbabi and L. L. Goddard, "Measurements of the refractive indices and thermo-optic coefficients of Si_3N_4 and SiOx using microring resonances," Opt. Lett. **38**, 3878–3881 (2013).
37. A. W. Elshaari, I. E. Zadeh, K. D. Jöns, and V. Zwiller, "Thermo-optic characterization of silicon nitride resonators for cryogenic photonic circuits," IEEE Photon. J. **8**, 1–9 (2016).
38. B. El-Kareh and L. N. Hutter, *Fundamentals of Semiconductor Processing Technology* (Springer, 2012).